Nanoscale

PAPER

CrossMark
← click for updates

Tuning the structure and habit of iron oxide mesocrystals†

Erik Wetterskog,*[a,b] Alice Klapper,[c] Sabrina Disch,[d] Elisabeth Josten,[c,e] Raphaël P. Hermann,[c,f] Ulrich Rücker,[c] Thomas Brückel,[c] Lennart Bergström[a] and German Salazar-Alvarez*[a]

A precise control over the meso- and microstructure of ordered and aligned nanoparticle assemblies, *i.e.*, mesocrystals, is essential in the quest for exploiting the collective material properties for potential applications. In this work, we produced evaporation-induced self-assembled mesocrystals with different mesostructures and crystal habits based on iron oxide nanocubes by varying the nanocube size and shape and by applying magnetic fields. A full 3D characterization of the mesocrystals was performed using image analysis, high-resolution scanning electron microscopy and Grazing Incidence Small Angle X-ray Scattering (GISAXS). This enabled the structural determination of *e.g.* multi-domain mesocrystals with complex crystal habits and the quantification of interparticle distances with sub-nm precision. Mesocrystals of small nanocubes (l = 8.6–12.6 nm) are isostructural with a body centred tetragonal (*bct*) lattice whereas assemblies of the largest nanocubes in this study (l = 13.6 nm) additionally form a simple cubic (*sc*) lattice. The mesocrystal habit can be tuned from a square, hexagonal to star-like and pillar shapes depending on the particle size and shape and the strength of the applied magnetic field. Finally, we outline a qualitative phase diagram of the evaporation-induced self-assembled superparamagnetic iron oxide nanocube mesocrystals based on nanocube edge length and magnetic field strength.

Introduction

Assemblies, multi-core beads, and mesocrystals composed of nanoparticles are currently being explored as candidates for new materials in a wide range of applications *e.g.* as sensors and photonic devices.[1–3] Particularly interesting is the emergence of novel and enhanced collective properties, *e.g.* optical and magnetic, in such ordered nanomaterials that go beyond the properties of the individual nanoparticles.[1,4–7] The intimate link between the arrangement of particles and their

properties[8–11] makes the assembly of mesostructured magnetic materials a highly relevant endeavour. Manipulation of the meso- and microstructure in magnetic nanoparticle assemblies can be achieved by applying magnetic fields that modify the range, magnitude and direction of the interactions between particles.[12–16] Recent developments in the manipulation and assembly of large superparamagnetic objects have provided responsive structured fluids and "colloidal molecules".[17–21] Subjecting ferrofluids to an applied magnetic field can result in instabilities that generate patterns at the macro- and microscale,[22–24] but compact ferrofluid assemblies typically lack long range order owing to a broad distribution of particle sizes and shapes. Developments in the synthesis of monodisperse and shape-controlled magnetic nanoparticles[25,26] have opened up a largely unexplored field of magnetic field-induced assembly of anisotropic nanoparticles. Notable landmarks include studies by Singh *et al.* on helical strands of nanocubes[12,27] and by Mehdizadeh Taheri *et al.* on in-solution assembly.[28] Anisotropic particles, in contrast to spherical particles, exhibit directional van der Waals interactions.[29,30] This directionality is a crucial aspect in the formation of mesocrystals,[31–34] which are defined as: oriented assemblies of nanoparticles displaying crystallographic texture.[35,36] In fact, significant effort has been devoted to assembly of anisotropic particles,[37,38] but there are only a

[a]*Department of Materials and Environmental Chemistry, Arrhenius Laboratory, Stockholm University, Sweden. E-mail: erik.wetterskog@angstrom.uu.se, gersal@protonmail.com*
[b]*Department of Engineering Sciences, Ångström Laboratory, Uppsala University, Sweden*
[c]*Jülich Centre for Neutron Science JCNS and Peter Grünberg Institut PGI, JARA-FIT, Forschungszentrum Jülich, 52425 Jülich, Germany*
[d]*Department of Chemistry, Universität zu Köln, 50939 Köln, Germany*
[e]*Helmholtz-Zentrum Dresden-Rossendorf, Institute of Ion Beam Physics and Materials Research, Bautzner Landstr. 400, 01328 Dresden, Germany*
[f]*Materials Science and Technology Division, Oak Ridge National Laboratory, Oak Ridge, 37831 Tennessee, USA*
†Electronic supplementary information (ESI) available: Morphological characterization of the nanocubes, further GISAXS analysis and indexed patterns, AFM images, additional SEM images, mesocrystal surface reconstruction using SEM images, and magnetic characterization. See DOI: 10.1039/c6nr03776c

handful of examples where the particle size has been varied systematically.[28,39,40] We will demonstrate that particles with neatly spaced size distributions are particularly valuable in evaluating the micro- and mesostructural effects resulting from the interplay between interparticle and external forces in nanoparticle assemblies.[41,42] Firstly, they allow us to study the connection between the shape and size of the particles with the 3D mesostructure of the arrays. Secondly, in the case of magnetic particles, the large difference between the particles' magnetic moments effectively provides a way to tune the dipolar interactions in applied magnetic fields, enabling control over both the mesostructure and the crystal habit.

In this work, we investigate the influence of particle size, shape and applied magnetic field on the formation of mesocrystals based on oleate-capped iron oxide nanocubes. We assembled nanocubes with four different edge lengths into highly ordered mesocrystals by controlled evaporation of the carrier solvent during drop-casting. We performed a full 3D characterization of the mesostructures using Grazing Incidence Small Angle X-ray Scattering (GISAXS) and determined the nanocube size and shape using Transmission Electron Microscopy (TEM). The interparticle distances in the mesocrystals were found to scale with the size and local curvature of the particles. The applied magnetic field strength influences the structure over several length scales and generates both single domain and complex multi-domain mesocrystals, and can even result in structures defined by ferrohydrodynamic instabilities. The micro- and mesostructure of the mesocrystals were analysed in detail by High Resolution Scanning Electron Microscopy (HRSEM) and image reconstruction techniques. Finally, we propose a qualitative micro- and mesostructural phase diagram of the nanocubes, based on edge length and applied magnetic field.

Experimental

Synthesis and characterization of iron oxide nanocubes

We synthesized highly monodisperse nanocubes (C086, C096, C126, C136) with edge lengths ($\pm\sigma_{std}$) of: 8.6 ± 0.5 nm, 9.6 ± 0.4 nm, 12.6 ± 0.8 nm, and 13.6 ± 0.8 nm by a modified version of the metal oleate route.[26] A detailed account of the preparation of the nanocubes is given elsewhere.[43] The as-synthesized nanocube dispersion is purified to a viscous nanocube paste with a solids content of ≈40–50 wt% iron oxide. We prepared the nanocube dispersions by diluting the paste in toluene followed by a brief 15 min ultrasonication and shaking. The nanocubes have a composition between γ-Fe_2O_3 and Fe_3O_4,[43,44] and a saturation magnetization of ≈60–65 emu g^{-1} (100 K). Magnetic measurements (using a Quantum Design MPMS) performed on deposited mesocrystals show that they are superparamagnetic with blocking (zero-field cooled cusp) temperatures well below room temperature ($T_B \approx$ 105, 125, 155 and 200 K, see Fig. S14†). High resolution TEM images show that all the nanocube samples have slightly rounded corners. We approximate the nanocube shape with a

superellipsoid.[45] In Cartesian coordinates the superellipsoid is given as: $|x|^n + |y|^n + |z|^n = (l/2)^n$ where l is the cube edge length and n is a real positive number. The superellipsoid exponent n is an alternative representation of the truncation parameter (τ) in our previous studies, where for an ideal cube $\tau = 0$ and for an ideal cuboctahedron $\tau = 1$.[30,46] The superellipsoid is a sphere for $n = 2$ and approaches a cube as $n \rightarrow \infty$. We determined n by measuring the diagonal-to-edge-length ratio (see ESI† for details). We found exponents around $n = 2.7$ and 2.9 for C086 and C126, and $n = 3.8$ and 3.7 for C096 and C136, respectively (see Fig. 1a). The parameter n is influenced by the ratio of excess sodium oleate/oleic acid used in the synthesis,[43] and decreases with aging upon long time storage of the nanocube dispersions.[46]

Grazing incidence small angle X-ray scattering (GISAXS) and self-assembly of iron oxide nanocubes

A custom evaporation chamber was designed to perform self-assembly experiments directly at the SOLEIL synchrotron beam-line SWING.[47] The chamber is equipped with two valves, a reservoir for toluene and a slot for an optional permanent magnet ($NdFe_{14}B$, $7 \times 5 \times 1$ cm) below the sample position (corresponding to μ_0H = 65 mT). The beam impinging on the sample had a size of 40 × 400 μm^2 and an energy of 11.0 keV. In order to minimize beam damage to the samples the exposure time was 50 ms per pattern. The detector features 4096 × 4096 px^2 with a pixel size of 165 μm and is located at 2.425 m from the sample. Single crystalline 1 × 1 cm^2 Si wafers washed with ethyl acetate followed by ethanol were used as substrates in the experiments. Note that assembly of the C086 nanocubes was performed *ex situ*, placing the substrate in a petri dish pre-saturated with toluene vapour. The magnetic field strength was measured at the sample position using a Gaussmeter, HIRST GM08. For the *ex situ* experiments (*i.e.* for C086), fields of μ_0H = 30 mT (a single $NdFe_{14}B$ magnet) and μ_0H = 200 mT (two $NdFe_{14}B$ magnets) were used. As described in several reports,[32,48] the lattice parameters vary slightly with the drying time of the mesocrystals. All lattice parameters reported in this work refer to fully dried out mesocrystals. GISAXS patterns of the dry mesocrystals were collected with a high-brilliance laboratory instrument, GALAXI.[49] The instrument is equipped with a Bruker AXS MetalJet X-ray source providing X-rays with a wavelength of 1.34 Å, and a beam size of 500 × 500 μm^2. The GISAXS patterns were acquired using an incident angle of 0.45° and a Dectris Pilatus 1 M detector with 981 × 1043 pixels of 172 μm pixel size placed at a sample–detector distance of 1.730 m.

Scanning electron microscopy (SEM)

Imaging of the self-assembled mesocrystals was performed using a JEOL 7000-F scanning electron microscopy (resolution: 1.5 nm at 15 keV). High resolution images were acquired in secondary electron (SE) mode at 15 keV. Low magnification images were acquired in backscatter (BS) mode. A working distance of 10 mm was used, ensuring excellent calibration of the image magnification. Side- and tilted (30°) view images of
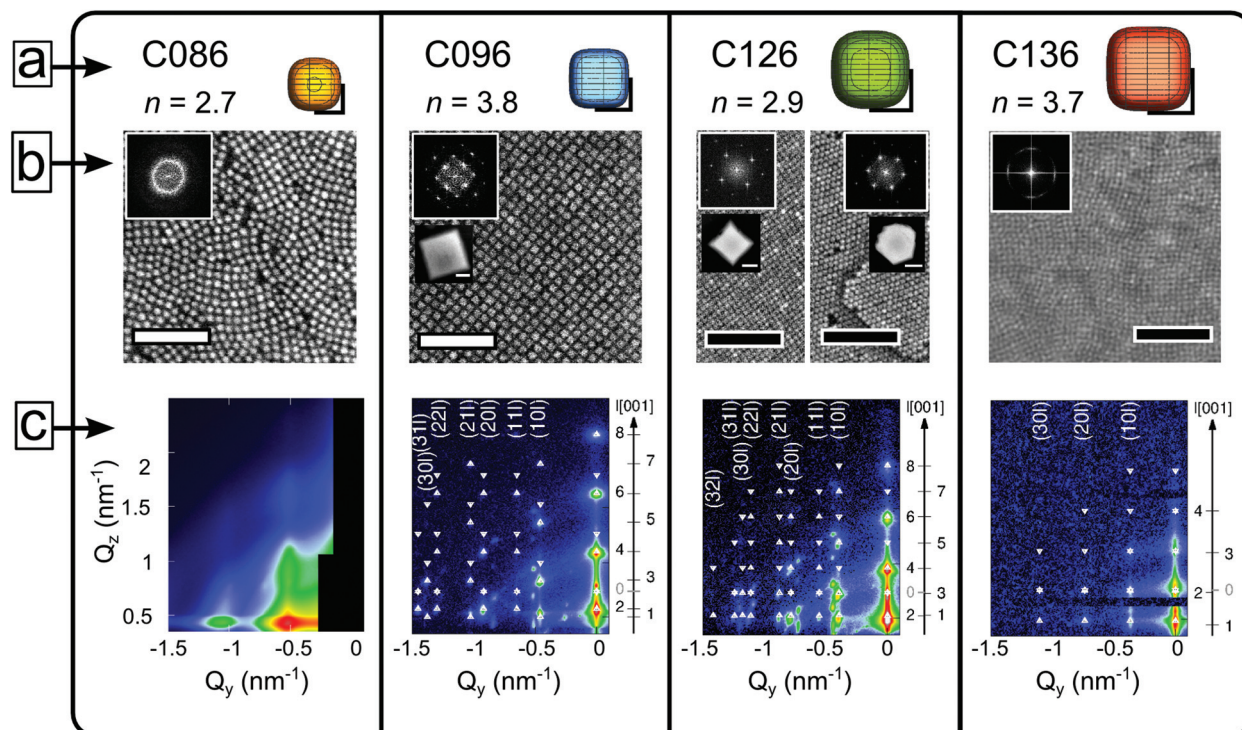
Fig. 1 SEM images and GISAXS patterns of zero-field assemblies of nanocubes with incremental edge lengths. (a) Sketch of the relative size and shape of the nanocubes in the mesocrystals (n denotes the superellipsoid exponent). (b) SEM images of the top surface of nanocube mesocrystals. For the C126-based mesocrystals we show examples of surface structures of two distinct growth orientations of the body centred tetragonal (*bct*) lattice. Scale bars: 100 nm (white), 200 nm (black). Insets in the top corner show the fast Fourier transform (FFT) of the SEM images. Insets below show the crystal habit associated with each mesostructure. Scale bar in insets: 1 μm. (c) GISAXS patterns with indexing corresponding to the $[001]_{MC}$-oriented mesostructures.

mesocrystals were acquired using a FEI Magellan 400 extreme high-resolution SEM (XHR-SEM, resolution 0.8 nm at 1 keV). Images were acquired at 3 keV in SE mode. Mesocrystal cross-sections were obtained by cleaving the Si substrate using a pair of pliers. A moderate UV/ozone treatment parallel to the substrate, perpendicular to the fracture surface, was necessary in order to acquire images of the highest quality.

Results and discussion

Influence of nanocube size and shape

Drop-casting a dilute dispersion of iron oxide nanocubes results in the formation of mesocrystals after evaporation of the carrier solvent.[50] Four different nanocube systems—C086, C096, C126, and C136—constitute the building blocks of the self-assembled materials in this work. Here, C stands for cube and *e.g.* 096 refers to the average edge length in Å (l = 9.6 nm). Nanocube contours were traced in HRTEM images and approximated to a 2D projection of a superellipsoid (with exponents n, see the Experimental section and ESI†). Models of the nanocubes are shown to scale in Fig. 1a. Arrays and mesocrystals composed of C086–C136 nanocubes assembled in a zero magnetic field are shown in Fig. 1b. The evaporation-induced self-assembly process involves spreading a droplet (20 μL) of a

dilute nanocube dispersion (2 mg mL^{-1}) over a Si substrate in a partially covered cell. The evaporation rate of the droplet was slowed down considerably by the use of a solvent reservoir within the cell compartment. This resulted in a time of ≈90 min from the application of the dispersion until emergence of the first Bragg spots in the GISAXS patterns (see Fig. 1c), which indicates nucleation of the first mesocrystals.

There is considerable difference in the translational order between the zero-field assemblies of the C086 and C096 nanocubes displayed in Fig. 1b. The C086 nanocubes form close packed arrays but lack long range order (*cf.* Debye–Scherrer ring in the inset of Fig. 1b) whereas the C096 nanocubes form large ordered mesocrystals (*cf.* spot pattern in the inset of Fig. 1b)—*i.e.* faceted, monodomain arrays of particles with a pronounced mesoscopic texture. The mesocrystals have flat top surfaces and uniform heights of 0.5–1 μm (see AFM images, Fig. S10†), suggesting that the vertical growth and thus the final thickness of the mesocrystals are limited by the thickness of the dispersion film.[50] Drop-casting the C126 nanocubes also produces mesocrystals under zero-field conditions (Fig. 1b). The C126-based mesocrystals display several morphologies: cuboidal, hexagonal and truncated triangular platelets. The different mesocrystal morphologies are also associated with a distinct symmetry at the top surface layer characterized by 4-fold (cuboids) or 2-fold (hexagonal/triangular platelets) rotation axes.

Evaporation-induced assembly of C136 nanocubes under zero-field conditions also generates mesocrystals, albeit with a considerably smaller domain size compared to mesocrystals produced from C096 and C126 (see Fig. 1b).

GISAXS patterns of nanocube mesocrystals assembled in zero-field are shown in Fig. 1c and corroborate the trend observed in the SEM images. The GISAXS pattern of a dispersion of C086 evaporated in zero-field displays broad reflections indicating a partially/short range ordered mesostructure of the dense packed array, as seen with SEM. In contrast, the C096 mesocrystals exhibit a highly ordered 3D mesostructure, clearly evidenced by the large number of sharp reflections in the scattering pattern. The structural analysis of the GISAXS patterns of C096-based mesocrystals reveals that they consist of a single mesostructure that has grown along two different orientations (see Fig. 2a and b). Analysis of the GISAXS data in Fig. 1c yields a body centered tetragonal (*bct*) lattice with $a = b < c$ and the $[001]_{MC}$-axis (the subscript denotes mesocrystal) parallel to the substrate normal. Additionally, we identify a second growth orientation (shown in Fig. 2b) corresponding to the $[101]_{MC}$-orientation of the same lattice (indexing of this orientation is found in Fig. S5, ESI†). Qualitative analysis of the reflection intensities in the GISAXS patterns (see Fig. S7 and discussion, ESI†) was used to estimate the ratio of growth orientations in the C096- and C126-based mesocrystals. We found that C096 favours growth along the $[001]_{MC}$-orientation (yielding square-shaped mesocrystals) whereas C126 favours growth in the $[101]_{MC}$-orientation corresponding to a hexagonal or a truncated triangular mesocrystal habit. The different crystal habits can be linked to morphological differences of the nanocubes (n_{C096}: 3.8 *vs.* n_{C126}: 2.9). Particles closer to an ideal cube tend to deposit face-on on the substrate and form a square basal plane whereas more rounded cubes with a higher degree of blunting of the edges and corners can rotate and deposit edge-on on the substrate (see Fig. 2b), thereby forming pseudo-hexagonal (2-fold) layers. This is in line with our previous findings, where we observed a shift in the symmetry of the horizontal layers (from 4-fold to 6-fold) after morphological aging of the C086 nanocubes to a more rounded shape.[46]

Remarkably, the GISAXS data in Fig. 1c (and Fig. S3, ESI†) reveal that the C086, C096, C126 systems and (in part) the C136 system are isostructural: each nanocube dispersion mesocrystallizes in a *bct* lattice. Similarly to the C096 system, the C126- and C136-based mesocrystals grow in two principal orientations: $[001]_{MC}$ and $[101]_{MC}$ with lattice parameters a, c, and a_r, c_r respectively (the subscript letter denotes rotation, see Fig. 2a and b). For the C136-based mesocrystals, there is a crossover from *bct* to *sc* (simple cubic) for the $[001]_{MC}$-oriented lattice. The $[101]_{MC}$-oriented structure remains isostructural with the other systems: a *bct* lattice with *c*-axis $\approx \sqrt{3}a_r$.

Orientational alignment of anisotropic nanocrystals has been reported to result from *e.g.* anisotropic van der Waals (vdW) interactions,[51,52] whereas the role of the surfactant has been less clear. In this work, owing to the ability to determine particle positions in the mesocrystal together with the precise characterization of the size and shape of the monodisperse
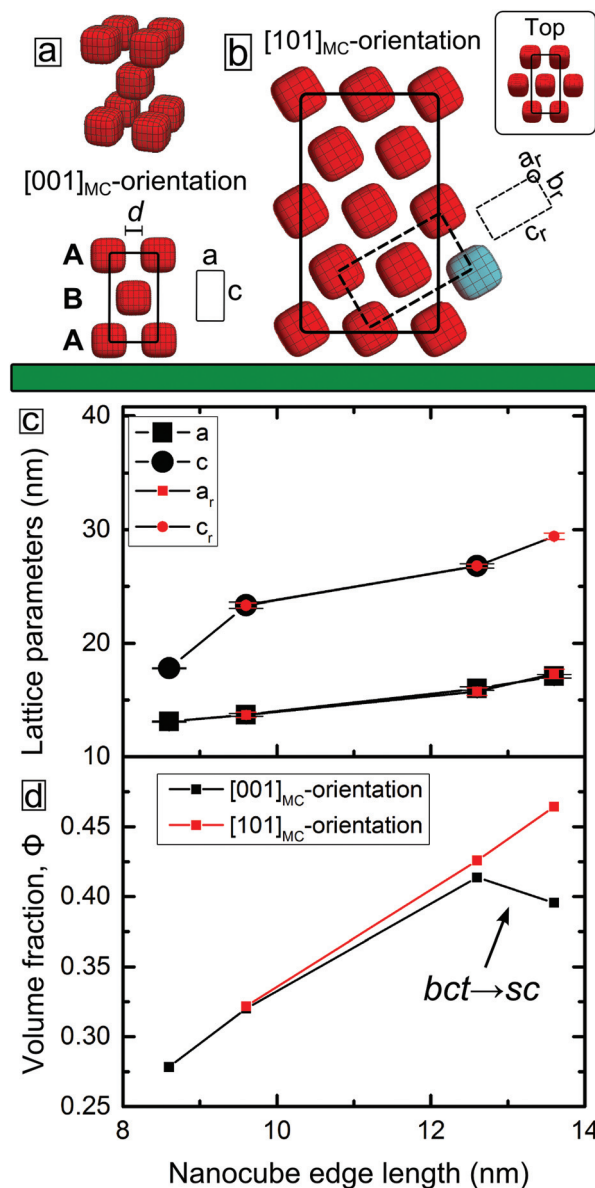

Fig. 2 Representation of the two growth orientations of the body centered tetragonal (*bct*) mesocrystal lattice and the variation of the lattice parameters and volume fraction with the nanocube edge length. (a) Structural model of the $[001]_{MC}$-oriented body centered tetragonal (*bct*) lattice. The face-to-face separation distance *d* is indicated. (b) Structural model of the $[101]_{MC}$-oriented *bct* lattice. The unit cell of a rotated (and distorted) *bct* unit cell with lattice parameters a_r, b_r and c_r is indicated by dashed lines. The larger unit cell corresponds to an orthorhombic unit cell (see ESI† for more information). Nanocubes in the top layer of the $[101]_{MC}$ oriented *bct* lattice are shown in the inset. The flat substrate is indicated by the green slab. (c) Plot of the *bct* lattice parameters corresponding to the $[101]_{MC}$ unit cell and to the rotated $[101]_{MC}$ unit cell. Note that for cubes larger than C086 there are two growth orientations with overlapping symbols. (d) Plot of the nanocube volume fraction *vs.* nanocube edge length in the self-assembled mesocrystals.

nanocubes, we can estimate the average separation distance of the nanocubes in the mesocrystals. The principal *bct* lattice parameters (a, a_r), and (c, c_r) *vs.* nanocube edge length (l) are

plotted in Fig. 2c. For comparison, we have included the lattice parameters of the C086-based mesocrystals where a small magnetic field of $\mu_0 H \approx 30$ mT has been applied to promote the formation of an ordered *bct* lattice.[30] For the C086–C126-based mesocrystals, we see that a depends linearly on the nanocube edge length l so that $a/\text{nm} \approx 7 + 0.7l$. This implies a gradual decrease from $\approx 4.5(2)$ to $3.4(2)$ nm of the separation distance between the faces of the nanocubes that correspond to two squeezed oleate capping layers: $d/\text{nm} = a - l = 7 - 0.3l$ (see Fig. S9†). This compression reflects the dynamic structure of the oleic acid double layer as a result of increasing vdW attraction between the nanocube faces. The oleic acid double layer appears to be incompressible beyond the minimum distance of ≈ 3.5 nm (*cf.* C126 and C136). This distance agrees reasonably well with twice the length of the L-form conformation of the oleic acid molecule (*cf.* β phase).[53]

Previous reports have suggested that a high (local) curvature increases the free volume for a grafted surfactant.[54] This allows for a high degree of surfactant chain interdigitation, which was experimentally confirmed by comparing laureate-capped films (2D) with particles (3D).[55] In the case of superellipsoids ($n > 2$), the Gaussian curvature approaches zero (are locally flat) at the centre of the face and increases rapidly towards its corners (shown in Fig. S2a, ESI†). In this logic, arrays of spherical particles (with $D_{\text{sph}} \approx l_{\text{cub}}$ and $n = 2$) should have shorter interparticle distances than nanocubes interacting face-to-face due a higher degree of interdigitation. Indeed, arrays composed of nanospheres with $D_{\text{sph}} = 9.2 \pm 0.6$ nm ($a_{\text{fcc}} = 17.5(1)$ nm)[46] display a significantly shorter interparticle distance of $d = 3.2(2)$ nm compared to the interlayer face-to-face distances of the C086- and C096-based mesocrystals: $d = 4.5(2)$–$4.1(2)$ nm.

Moreover, we notice that the two sets of nanocubes with more rounded morphologies, *i.e.* C086 and C126 ($n = 2.7$ and 2.9, respectively), form *bct* lattices with "short" c-axes $\approx 2l$ in each case implying a short intra-layer distance <1 nm in the tetragonal ABAB stacking (see Fig. 2a). The short intra-layer distance relates to interacting nanocube corners, *i.e.* surfaces with high local curvature that are expected to result in a high degree of interdigitation. The effective thickness of the "first" (A) nanocube layer (including the surfactant layers at the face of the cuboids corresponding to ≈ 4.5–3.5 nm) means that the nanocubes in the B-layer sit slightly recessed in the holes of the square lattice of the A-layer (see Fig. 2a). From a simple geometrical view, an increase of n results in a concomitant decrease of the hole size in the A-layer (see Fig. S2b, ESI†), thereby "pushing" out the particle in the B-layer. Indeed, the assembly of the relatively small, but less rounded C096 ($n = 3.8$) results in a *bct* lattice with $c > 2l$ and a slightly longer intra-layer distance of ≈ 2 nm.

For the largest and relatively less rounded C136 nanocubes ($n = 3.7$) we observe two distinct mesostructures: a $[101]_{\text{MC}}$-oriented *bct* lattice (see Fig. S5†) and a $[001]_{\text{MC}}$-oriented *sc* lattice (with $a_{\text{sc}} = a_{\text{bct}}$, see Fig. 1) which is not observed for the other particle sizes. In a previous study,[30] we attributed the preference for a *bct* lattice over a *sc* lattice to the exceptionally short interlayer corner-to-corner distance (≈ 0.6 nm) between

the nanocubes in C086-based *bct* mesocrystals. As discussed above, the increase of n (which relates to a decrease in the degree of truncation) yields a longer c-axis, due to an associated decrease of the interstitial hole volume in the A-layer. This, in turn, will weaken the interlayer attraction and favour the transition to a *sc* structure. The experimental observations made in this work therefore confirm the previously suggested stability diagram[30] derived for the C086 nanocubes. Compared to the C086 system, we observe an elongation of the c-axis with the decrease in truncation (*cf.* C096). For the largest cubes in this study (C136), the concomitant reduction of the interstitial hole volume relative to the cube volume leads to the formation of a simple cubic lattice. Interestingly, the simple cubic arrangement is actually less dense than the corresponding *bct* lattice: 40(2) *vs.* 46(3)% (see Fig. 2d).

The co-existence of two structures (*bct*, *sc*) in the C136 nanocube system suggests that their lattice energies are very close. We speculate that the structural divergence with respect to substrate orientation relates to the initial growth conditions. Assuming layer-by-layer growth, the hole volume of the 4-fold layers (see Fig. S2b, ESI†) is small compared to the nanocube, effectively rendering the surface flat. In contrast, the top layer of the $[101]_{\text{MC}}$-oriented *bct* lattice (see Fig. 2b) is a surface with a much larger topographic roughness that can accommodate cubes in the next layer. The isostructurality of the nanocube mesocrystal system, together with the micro- and mesostructural diversity presented here, highlights its structural richness and sensitivity to small variations in particle size and shape.

Mesocrystal growth in magnetic fields

The mesostructural order of the C086 nanocubes can be improved by applying a magnetic field of $\mu_0 H_{\text{app}} = 30$ mT (see Fig. S3, ESI†).[15,30] Nonetheless, the effect of magnetic fields on the mesocrystal habit has remained largely unknown. In this section, we investigate the structural effects of applied magnetic fields for the systems of larger magnetic nanocubes that readily mesocrystallize under zero-field conditions. Fig. 3 compares representative SEM images of the C096- and C126-based mesocrystal morphologies assembled in zero-field and in a moderately strong magnetic field ($\mu_0 H_{\text{app}} = 65$ mT) applied perpendicular to the substrate. Apart from the applied magnetic field, the assembly experiments were performed under identical conditions.

Mesocrystallization with or without an applied magnetic field exhibits two notable differences. For the C096 nanocubes, the habits of the mesocrystals change drastically, from square to irregular branched shapes, in particular 4-pointed stars (see Fig. 3a and b and S11†). The GISAXS patterns reveal a change in the preferred growth orientation from $[001]_{\text{MC}}$ in zero field to $[101]_{\text{MC}}$ when the drop casting has been performed in a field of 65 mT (see Fig. S7 and discussion, ESI†). A similar field-assisted morphological crossover is observed for the C126 system (see Fig. 3c and d), although the in-field assembled mesocrystals are slightly smaller and less branched compared to the C096-based mesocrystals. For the C126 system the GISAXS analysis suggests a crossover from $[101]_{\text{MC}}$ under zero-
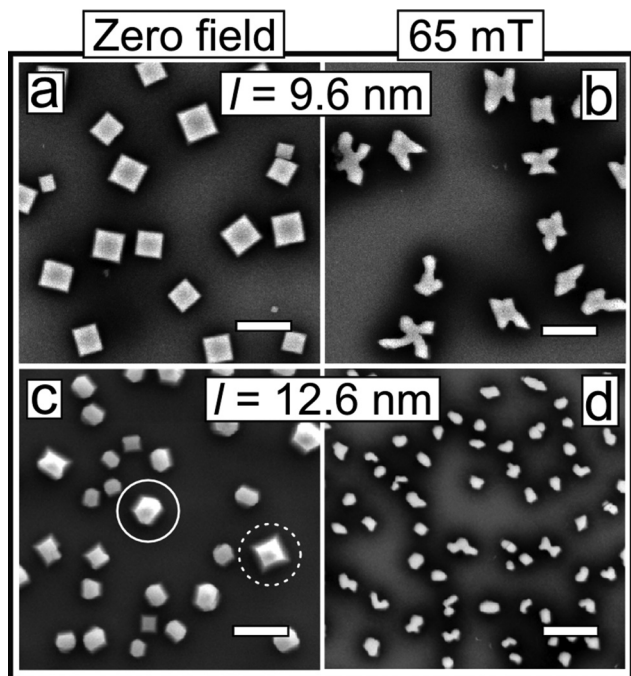
Fig. 3 Comparison of the mesocrystal microstructure in zero field and in-field ($\mu_0 H_{app}$ = 65 mT). Mesocrystals composed of (a, b) C096 and (c, d) C126 iron oxide nanocubes. The white circles highlight the two different mesocrystal morphologies found in the zero-field assemblies of the C126 nanocubes, *i.e.* hexagonal (solid line) and square platelets (dashed line). Scale bars: 5 μm.

field conditions to a slight preference for $[001]_{MC}$ for assembly at 65 mT. Analysis of HRSEM images also indicates a similar change in the growth direction (see Fig. S12†).

Two examples of irregularly shaped C096-based mesocrystals are shown in the tilted view in Fig. 4a and b. A central cross-section of a mesocrystal shown in Fig. 4c (here viewed
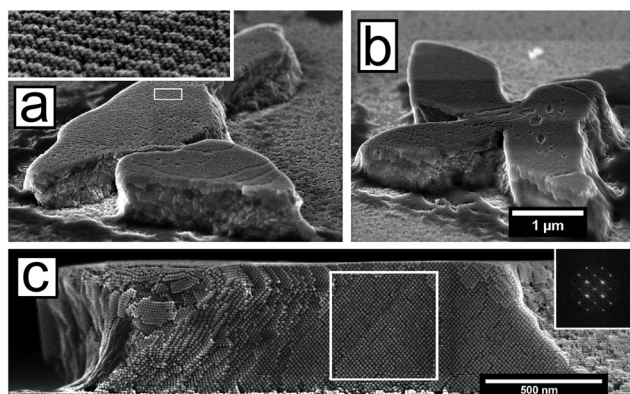
Fig. 4 Tilted views and cross-section of C096-based mesocrystals assembled in a field of $\mu_0 H_{app}$ = 65 mT. (a, b) Tilted views (30°) of two mesocrystals with branched morphologies. The inset in (a) shows a magnification of the part of the crystal displaying a wave-like surface structure highlighted by the white rectangle. (c) Fracture surface, revealing the internal structure of a mesocrystal. The FFT inset corresponds to the area inside the white square.

parallel to the substrate) clearly demonstrates a high degree of order throughout the volume of the mesocrystal. The peculiar microstructures (a majority of them being 4-pointed stars) of the magnetic field-assembled mesocrystals originate from the intergrowth of several mesostructural domains that were analysed in detail using HRSEM.

Fig. 5a shows a mesocrystal where the different domains have been coloured according to the plane group symmetry of the top layer, with either a 2-fold (*pmm*) or 4-fold (*p4mm*) symmetry, *cf.* the green and blue models in Fig. 5b. The reciprocal lattice distances derived from FFT patterns show that the domains with 4-fold (*p4mm*) symmetry correspond to the $(001)_{MC}$ cleavage planes of the previously described *bct* lattice. The lattice parameter obtained from the analysis of the FFT of the SEM image, a = 13.5(3) nm, is in good agreement with that from GISAXS, a = 13.70(1) nm. Particles in domains with a 2-fold (*pmm*) symmetry have characteristic nearest neighbour distances of 13.5(3) nm and 15.2(3) nm. These distances match the $(101)_{MC}$ cleavage planes of the same *bct* lattice (see Fig. 5b), in perfect agreement with the GISAXS analysis. The co-existence of several structurally correlated domains within a single mesocrystal is further highlighted in Fig. 5c. The HR-SEM image shows the lattice of a 4-point mesocrystal star (Fig. 5d) featuring two epitaxial grain boundaries. Quite remarkably for the C096 mesocrystal system, the grain boundaries between the $[001]_{MC}$ and the $[101]_{MC}$ oriented domains are coherent (*cf.* side view, Fig. 5b), producing an interface that is almost free of strain. The coherent grain boundaries of the C096-based mesocrystals result from the particular dimensions of the *bct* unit cell: $\sqrt{c^2 + a^2}/2 = c \rightarrow c/a = \sqrt{3}$, see Fig. 5b and c. Moreover, intergrown $[001]_{MC}$ and $[101]_{MC}$-domains of the C096- and C126-based mesocrystals are always found in the same relative (in-plane) orientation (shown in Fig. 5b). The observed preference for the $(001)_{MC}$ and $(101)_{MC}$ surface structures can be explained by noting that they are the two densest surface planes of a *bct* lattice with $a = b < c$.

At the particle level, a rotation of anisotropic nanocrystals can result from alignment of the magnetic easy axes of the nanocubes in the direction of the applied magnetic field. This gives rise to a global crystallographic texture.[56] Electron diffraction from thin $[001]_{MC}$-oriented C096 (*bct*) multilayers confirms the expected <100>-orientation of the spinel crystal axes with the substrate normal for mesocrystals with a 4-fold (*p4mm*) symmetry.[43] For C096- (and C126)-based mesocrystals the particle volume fraction curves of the $[001]_{MC}$ and $[101]_{MC}$-lattices overlap (see Fig. 2d), indicating that the nanocube orientation is maintained relative to the mesocrystal unit cell.[46] Thus, rotation of a *bct* mesocrystal from a $[001]_{MC}$- to a $[101]_{MC}$-orientation will cause the <110>$_{NC}$-crystal axes to lie approximately in the field direction, suggesting that the re-orientation of C096-based mesocrystals is assisted by alignment of the nanocubes' magnetic easy axes with the applied magnetic field.[44,56,57] Indeed, in the recent study by Mehdizadeh Taheri *et al.*,[28] a large applied magnetic field of $\mu_0 H$ = 1 T was found to directly determine the growth orientation for solution growth of nanocube mesocrystals.
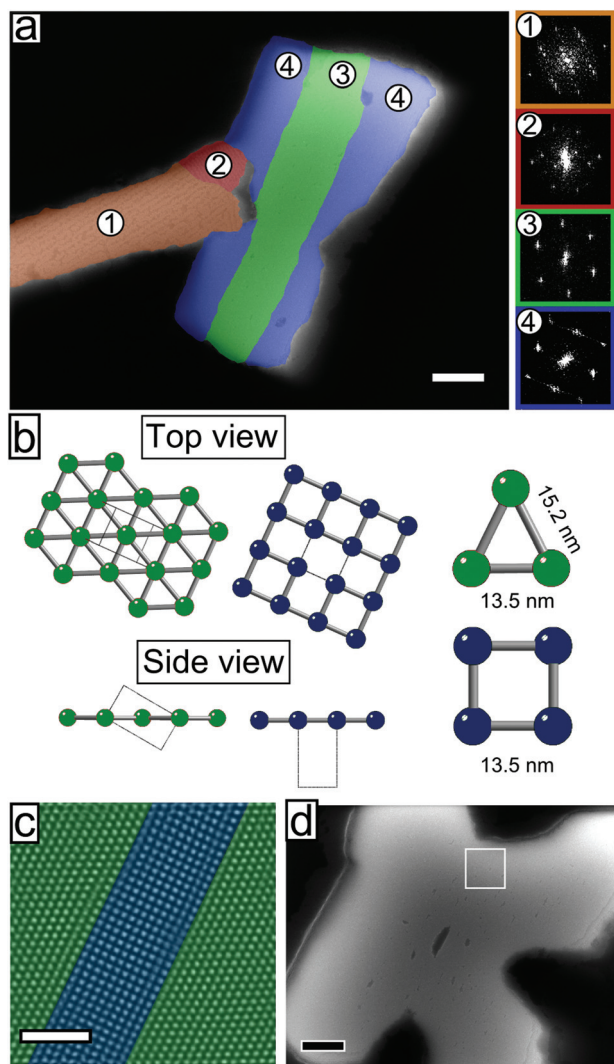
Fig. 5 Structural analysis of the multidomain C096-based mesocrystals assembled in a magnetic field ($\mu_0 H_{app}$ = 65 mT). (a) Color-coded/numbered SEM images of multidomain mesocrystals, where each color/number corresponds to the symmetry of the mesocrystal top layer. The FFTs of the SEM images correspond to the top layer of the color-coded/numbered areas. Scale bar: 500 nm. (b) Surface structures with a 2- and 4-fold rotation symmetry correspond to the $(101)_{MC}$ and $(100)_{MC}$ cleavage planes of a *bct* cell with lattice parameters: $a = b$ = 13.5 and c = 23.8 nm. The orientation of the unit cell is shown for clarity. (c) SEM image of two grain-boundaries (scale bar: 100 nm) at the area marked in (d), a star-shaped multidomain mesocrystal. The image has been FFT-filtered for clarity. Scale bar: 500 nm.

Ferrohydrodynamic instabilities

A large number of mesocrystals with elongated shapes such as the crystals shown in Fig. 4a (and inset) and Fig. 5a (orange domain) display rippled surfaces, which result in a superstructure with a pitch that is approximately commensurate with the mesocrystal *bct* lattice. A reconstruction of the mesocrystal surface using a computer generated model (see Fig. S13, ESI†) suggests a sinusoidal perturbation of the first few layers of the mesocrystal surface. We have previously

observed similar superstructures resulting from a periodic ordering of stacking faults.[46] Although occurring at much smaller length scales, the rippled surfaces shown in this work bear a resemblance to (macroscopic) surface waves observed in experiments with ferrofluid surfaces subjected to magnetic fields.[58,59]

For the C136, and to a lesser extent for the C126 nanocubes, assembly in an intermediate field of $\mu_0 H_{app}$ = 65 mT results in the formation of structures with a noticeable global anisotropy *i.e.* arrays of oriented mesocrystals (see Fig. 6a). In areas with a relatively high concentration (*i.e.* the substrate edges),[60] arrays of mesoscopic pillars form (Fig. 6b). For the C136 nanocubes, the magnetic field guiding effect is so considerable that it can be observed directly in the scattering experiments.

Fig. 6c shows a GISAXS pattern of the zero-field assemblies of the C136 nanocubes, displaying a *sc* lattice. Assembly under $\mu_0 H_{app}$ = 65 mT (Fig. 6d) causes the GISAXS patterns of the in-field assembled C136 to smear out in broad rings. Below the dashed Yoneda line[61] there is a SAXS pattern originating from the transmission of X-rays through the substrate. The transmission SAXS pattern displays a texture with Bragg spots smeared in the in-arc direction and is slightly tilted ($\approx 5°$, see Fig. 6e) with respect to the substrate reference frame/Yoneda
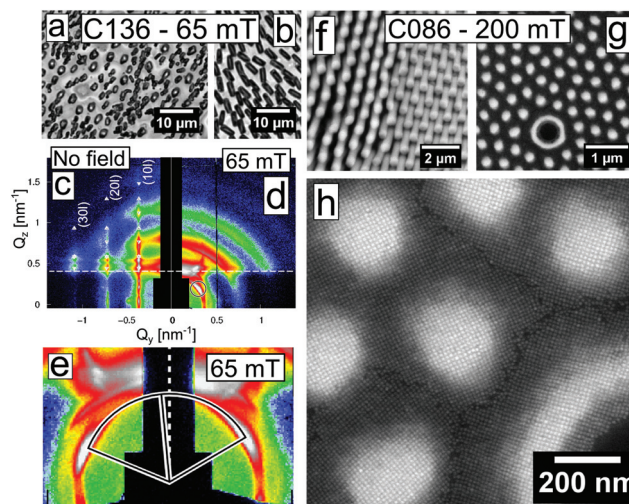

Fig. 6 Ferrohydrodynamic instabilities in nanocube assemblies. Light microscopy image showing (a) arrays of oriented mesocrystals and (b) collapsed pillars composed of C136 nanocubes assembled in a field of $\mu_0 H_{app}$ = 65 mT. GISAXS patterns of C136 assembled under (c) zero field, indexed to a *sc* lattice and (d) under a magnetic field of $\mu_0 H_{app}$ = 65 mT, destroying the mesoscale ordering with respect to the substrate reference plane. One reflection of the SAXS component is highlighted beneath the Yoneda line. (e) Detail of the central portion of the SAXS component shown in (d). The tilt angle ($\approx 5°$) relative to the substrate is highlighted. (f–h) Assemblies of C086 in a strong magnetic field ($\mu_0 H_{app}$ = 200 mT). Hexagonal array of (f) longer pillars and (g) protrusions composed of nanocubes. A toroidal nanocube structure can be seen in (g). (h) A magnified portion of the area in (g), showing the ordering in the torus and the protrusions near the substrate surface. Note that the centre of the torus is devoid of nanocubes.

line. The tilt angle represents the angle between the stray field and the substrate caused by a slight misalignment between the substrate and the centre of the magnet. The appearance of a tilted SAXS pattern and the complete loss of the spotted GISAXS pattern for the C136-based mesocrystals under an applied field represent a crossover where the field and its gradient, rather than the substrate orientation, define the mesocrystal growth orientations. In high fields ($\mu_0 H_{app}$ = 200 mT) we found that the smallest nanocubes (C086) form μm-sized pillars in a nearly hexagonal array and an interpillar spacing roughly equal to the average pillar diameter (see Fig. 6f and g). The pillars vary in height over the substrate surface, and can be found ranging from small protrusions to pillars with large aspect ratios, occasionally hollow with void interiors. HRSEM images reveal that the translational order of the nanocrystals in the base of these pillars is well-defined (see Fig. 6h). Further away from the substrate, the structural coherence is lost due to cracking and/or bending of the mesoscopic pillars. The loss of structural coherence results in GISAXS patterns with broad Debye–Scherrer rings (see Fig. S8, ESI†).

The field-response of magnetic nanoparticles can be understood in the framework of the Rosensweig (or normal-field) instabilities, which occur when a ferrofluid is subjected to a vertical magnetic field.[22–24] Above a certain critical field strength, the fluid layer orders into a hexagonal array of pillars as a result of the competition between magnetic and surface forces. The characteristic spacing in the hexagonal pattern (instability wavenumber) follows an exponential decay with the thickness of the ferrofluid layer and a logarithmic increase with the applied field.[62] Consequently, the large wavenumbers of the instability-generated patterns in Fig. 6 result from the limited critical film thickness in a typical drop-casting experiment, i.e. of the order of a few micrometres, and the relatively large applied field, i.e., $\mu_0 H_{app}$ = 65 mT. Similar field-induced patterns formed by spherical Co and γ-Fe_2O_3 and octahedral Fe_3O_4 nanoparticles have been investigated in some depth by the Pileni[63,64] and Li et al.[40] groups.

We suggest a qualitative phase diagram (shown in Fig. 7) that summarizes our observations for the iron oxide nanocube in this work. In the case of small nanocubes ($l \approx 8.5$ nm) the application of a weak magnetic field during drop casting assists the formation of assemblies with long range order. Mehdizadeh Taheri et al. speculated on the existence of a lower-size limit for the assembly of iron oxide nanocubes,[28] a limit which ultimately should depend on a number of other experimental parameters e.g. particle concentration, applied field, surfactant coverage, and chain length. Nonetheless, nanocubes with edge lengths between 9.6 and 13.6 nm form ordered single-domain mesocrystals in zero field. Upon the application of a moderately strong magnetic field (65 mT), nanocubes with edge lengths of 9.6 nm and 12.6 nm assemble into multidomain mesocrystals, composed of smaller mesocrystals in certain configurations. The small mesocrystals are fused over coherent grain boundaries and oriented primarily in two ways: with either $[101]_{MC}$ or $[001]_{MC}$ perpendicular to the substrate. We suggest that this reorientation follows the align-
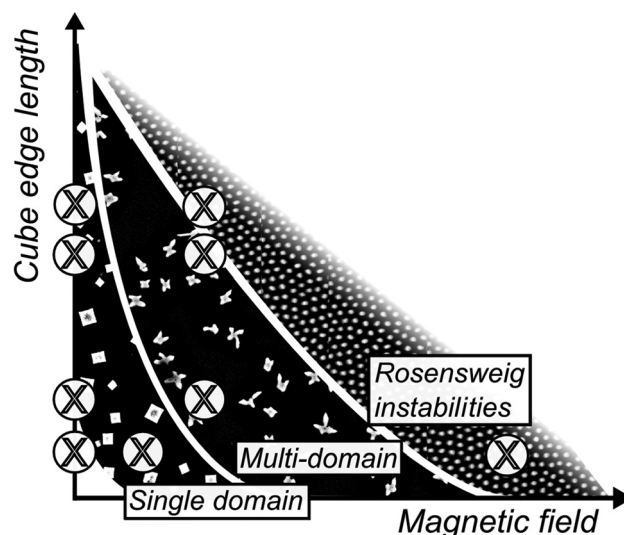

Fig. 7 A qualitative phase diagram for the formation of mesocrystals composed of oleate-capped iron oxide nanocubes in a perpendicular applied magnetic field. The crosses represent experimental observations of this work.

ment of the magnetic easy axes of the iron oxide nanocubes with the applied magnetic field. When a strong magnetic field (200 mT) is applied to the smallest nanocubes (l = 8.6 nm) we observe the onset of Rosensweig instabilities that results in the formation of hexagonal patterns of nanocube pillars.

Conclusions

In summary, we have investigated the micro- and mesostructure of self-assembled mesocrystals composed of nanocubes with different edge lengths in the absence and presence of an applied magnetic field. 3D structural characterization of the mesocrystals using GISAXS together with a rigorous morphological characterization of the nanocubes yields interparticle distances in the mesocrystals with sub-nm precision. The nanocube mesocrystals are isostructural and crystallize in a body centred tetragonal (bct) lattice with $a = b < c$ along two principal growth orientations: $[001]_{MC}$ and $[101]_{MC}$. In the case of the largest nanocubes in this study, there is a crossover to a simple cubic (sc) lattice for the $[001]_{MC}$ oriented structure. We found a linear dependence of the face-to-face intercube distances with nanocube edge length, whereas in other configurations the interparticle distances vary significantly with the local particle curvature. For nanocubes of intermediate edge length the application of a magnetic field of 65 mT yields multidomain mesocrystals. These have complex shapes, primarily 4-point stars, resulting from the intergrowth of $[001]_{MC}$ and $[101]_{MC}$ domains. For small nanocubes in large fields or for large nanocubes in intermediate fields, we observe the formation of aligned mesocrystals and ferrohydrodynamic instabilities. This represents a crossover where the magnetic field rather than the substrate directs and orients the growth

of nanocube structures. We summarize our conclusions in a qualitative phase diagram which outlines the preparation of mesocrystals and arrays with tunable micro- and mesostructure. This level of structural control over several length scales can facilitate the successful design of novel devices, *e.g.* magnetic on-chip structures, with tailored properties for future applications.

Author contributions

E. W., G. S. A., and L. B. conceived the study. E. W. synthesized the iron oxide nanocubes. E. J., U. R., and T. B. designed and built the experimental chamber for *in situ* GISAXS measurements. E. W., A. K., E. J., R. P. H., and G. S. A. performed the assembly/*in situ* GISAXS experiments. E. W. and S. D. performed *ex situ* drop-casting experiments. E. W. acquired and analysed the microscopy images. A. K. and S. D. analysed the X-ray scattering data. E. W. and G. S. A. wrote the manuscript. All authors commented on the manuscript.

Acknowledgements

References

1 Z. Nie, A. Petukhova and E. Kumacheva, *Nat. Nanotechnol.*, 2010, **5**, 15–25.

2 S. Liu and Z. Tang, *J. Mater. Chem.*, 2010, **20**, 24–35.

3 Z. Lu and Y. Yin, *Chem. Soc. Rev.*, 2012, **41**, 6874–6887.

4 S. Singamaneni, V. N. Bliznyuk, C. Binek and E. Y. Tsymbal, *J. Mater. Chem.*, 2011, **21**, 16819–16845.

5 L. Wang, L. Xu, H. Kuang, C. Xu and N. A. Kotov, *Acc. Chem. Res.*, 2012, **45**, 1916–1926.

6 K. L. Young, M. B. Ross, M. G. Blaber, M. Rycenga, M. R. Jones, C. Zhang, A. J. Senesi, B. Lee, G. C. Schatz and C. A. Mirkin, *Adv. Mater.*, 2014, **26**, 653–659.

7 B. Faure, E. Wetterskog, K. Gunnarsson, E. Josten, R. P. Hermann, T. Brückel, J. W. Andreasen, F. Meneau, M. Meyer, A. Lyubartsev, L. Bergström, G. Salazar-Alvarez and P. Svedlindh, *Nanoscale*, 2013, **5**, 953–960.

8 S. Mørup, M. F. Hansen and C. Frandsen, *Beilstein J. Nanotechnol.*, 2010, **1**, 182–190.

9 J. A. De Toro, P. S. Normile, S. S. Lee, D. Salazar, J. L. Cheong, P. Muñiz, J. M. Riveiro, M. Hillenkamp, F. Tournus, A. Tamion and P. Nordblad, *J. Phys. Chem. C*, 2013, **117**, 10213–10219.

10 M. Varón, M. Beleggia, T. Kasama, R. J. Harrison, R. E. Dunin-Borkowski, V. F. Puntes and C. Frandsen, *Sci. Rep.*, 2013, **3**, 1234.

11 K. Yamamoto, C. R. Hogg, S. Yamamuro, T. Hirayama and S. A. Majetich, *Appl. Phys. Lett.*, 2011, **98**, 072509.

12 G. Singh, H. Chan, T. Udayabhaskararao, E. Gelman, D. Peddis, A. Baskin, G. Leitus, P. Král and R. Klajn, *Faraday Discuss.*, 2015, **181**, 403–421.

13 A. Weddemann, F. Wittbracht, B. Eickenberg and A. Hütten, *Langmuir*, 2010, **26**, 19225–19229.

14 V. Bliznyuk, S. Singamaneni, S. Sahoo, S. Polisetty, X. He and C. Binek, *Nanotechnology*, 2009, **20**, 105606.

15 A. Ahniyaz, Y. Sakamoto and L. Bergström, *Proc. Natl. Acad. Sci. U. S. A.*, 2007, **104**, 17570–17574.

16 M. Grzelczak, J. Vermant, E. M. Furst and L. M. Liz-Marzán, *ACS Nano*, 2010, **4**, 3591–3605.

17 A. F. Demirörs, P. P. Pillai, B. Kowalczyk and B. A. Grzybowski, *Nature*, 2013, **2**, 3–7.

18 M. Ye, S. Zorba, L. He, Y. Hu, R. T. Maxwell, C. Farah, Q. Zhang and Y. Yin, *J. Mater. Chem.*, 2010, **20**, 7965–7969.

19 J. W. Tavacoli, P. Bauër, M. Fermigier, D. Bartolo, J. Heuvingh and O. du Roure, *Soft Matter*, 2013, **9**, 9103–9110.

20 M. Wang, L. He and Y. Yin, *Mater. Today*, 2013, **16**, 110–116.

21 V. Malik, A. V. Petukhov, L. He, Y. Yin and M. Schmidt, *Langmuir*, 2012, **28**, 14777–14783.

22 J. L. Neuringer and R. E. Rosensweig, *Phys. Fluids*, 1964, **7**, 1927.

23 R. E. Rosensweig, *Ferrohydrodynamics*, Cambridge University Press, 1985.

24 A. G. Boudouvis, J. L. Puchalla, L. E. Scriven and R. E. Rosensweig, *J. Magn. Magn. Mater.*, 1987, **65**, 307–310.

25 S. Sun, H. Zeng, D. B. Robinson, S. Raoux, P. M. Rice, S. X. Wang and G. Li, *J. Am. Chem. Soc.*, 2004, **126**, 273–279.

26 J. Park, K. An, Y. Hwang, J.-G. Park, H.-J. Noh, J.-Y. Kim, J.-H. Park, N.-M. Hwang and T. Hyeon, *Nat. Mater.*, 2004, **3**, 891–895.

27 G. Singh, H. Chan, A. Baskin, E. Gelman, N. Repnin, P. Kral and R. Klajn, *Science*, 2014, **345**, 1149–1153.

28 S. Mehdizadeh Taheri, M. Michaelis, T. Friedrich, B. Förster, M. Drechsler, F. M. Römer, P. Bösecke, T. Narayanan, B. Weber, I. Rehberg, S. Rosenfeldt and

S. Förster, *Proc. Natl. Acad. Sci. U. S. A.*, 2015, **112**, 14484–14489.

29 J. C. Hopkins, R. Podgornik, W. Ching, R. H. French and V. A. Parsegian, *J. Phys. Chem. C*, 2015, **119**, 19083–19094.

30 S. Disch, E. Wetterskog, R. P. Hermann, G. Salazar-Alvarez, P. Busch, T. Brückel, L. Bergström and S. Kamali, *Nano Lett.*, 2011, **11**, 1651–1656.

31 P. Simon, E. Rosseeva, I. A. Baburin, L. Liebscher, S. G. Hickey, R. Cardoso-Gil, A. Eychmüller, R. Kniep and W. Carrillo-Cabrera, *Angew. Chem., Int. Ed.*, 2012, **51**, 10776–10781.

32 K. Bian, J. J. Choi, A. Kaushik, P. Clancy, D.-M. Smilgies and T. Hanrath, *ACS Nano*, 2011, **5**, 2815–2823.

33 J. Zhang, Z. Luo, Z. Quan, Y. Wang, A. Kumbhar, D.-M. Smilgies and J. Fang, *Nano Lett.*, 2011, **11**, 2912–2918.

34 R. Zheng, H. Gu, B. Xu, K. Fung, X. X. Zhang and S. P. Ringer, *Adv. Mater.*, 2006, **18**, 2418–2421.

35 L. Bergström, E. V. Sturm (née Rosseeva), G. Salazar-Alvarez and H. Cölfen, *Acc. Chem. Res.*, 2015, **48**, 1391–1402.

36 H. Cölfen and M. Antonietti, *Angew. Chem., Int. Ed.*, 2005, **44**, 5576–5591.

37 S. C. Glotzer and M. J. Solomon, *Nat. Mater.*, 2007, **6**, 557–562.

38 Z. Quan and J. Fang, *Nano Today*, 2010, **5**, 390–411.

39 C. Chang, H. Wu, C. Kuo and M. H. Huang, *Chem. Mater.*, 2008, **20**, 7570–7574.

40 L. Li, Y. Yang, J. Ding and J. Xue, *Chem. Mater.*, 2010, **22**, 3183–3191.

41 Y. Min, M. Akbulut, K. Kristiansen, Y. Golan and J. Israelachvili, *Nat. Mater.*, 2008, **7**, 527–538.

42 K. J. M. Bishop, C. E. Wilmer, S. Soh and B. A. Grzybowski, *Small*, 2009, **5**, 1600–1630.

43 E. Wetterskog, M. Agthe, A. Mayence, J. Grins, D. Wang, S. Rana, A. Ahniyaz, G. Salazar-Alvarez and L. Bergström, *Sci. Technol. Adv. Mater.*, 2014, **15**, 055010.

44 E. Wetterskog, C.-W. Tai, J. Grins, L. Bergström and G. Salazar-Alvarez, *ACS Nano*, 2013, **7**, 7132–7144.

45 P. Linse, *Soft Matter*, 2015, **11**, 3900–3912.

46 S. Disch, E. Wetterskog, R. P. Hermann, D. Korolkov, P. Busch, P. Boesecke, O. Lyon, U. Vainio, G. Salazar-Alvarez, L. Bergström and T. Brückel, *Nanoscale*, 2013, **5**, 3969–3975.

47 E. Josten, RWTH Aachen University, Germany, 2015.

48 T. Hanrath, J. J. Choi and D.-M. Smilgies, *ACS Nano*, 2009, **3**, 2975–2988.

49 E. Kentzinger, M. Krutyeva and U. Rücker, *J. Large-scale Res. Facil. JLSRF*, 2016, **2**, A61.

50 M. Agthe, E. Wetterskog, J. Mouzon, G. Salazar-Alvarez and L. Bergström, *CrystEngComm*, 2014, **16**, 1443–1450.

51 D. M. Dryden, J. C. Hopkins, L. K. DeNoyer, L. Poudel, N. F. Steinmetz, W. Y. Ching, R. Podgornik, A. Parsegian and R. H. French, *Langmuir*, 2015, **31**, 10145–10153.

52 A. Parsegian, *van der Waals forces: a handbook for biologists, chemists, engineers, and physicists*, Cambridge University Press, New York, 2006.

53 F. Kaneko, K. Yamazaki, K. Kitagawa, T. Kikyo, M. Kobayashi, Y. Kitagawa, Y. Matsuura, K. Sato and M. Suzuki, *J. Phys. Chem. B*, 1997, **101**, 1803–1809.

54 M. R. Farrow, P. J. Camp, P. J. Dowding and K. Lewtas, *Phys. Chem. Chem. Phys.*, 2013, **15**, 11653–11660.

55 V. Patil, K. S. Mayya, S. D. Pradhan and M. Sastry, *J. Am. Chem. Soc.*, 1997, **7863**, 9281–9282.

56 F. Gazeau, J. Bacri, F. Gendron, R. Perzynski, Y. Raikher, V. Stepanov and E. Dubois, *J. Magn. Magn. Mater.*, 1998, **186**, 175–187.

57 H.-C. Wu, O. Mauit, C. Ó. Coileáin, A. Syrlybekov, A. Khalid, A. Mouti, M. Abid, H.-Z. Zhang, M. Abid and I. V. Shvets, *Sci. Rep.*, 2014, **4**, 7012.

58 J. Browaeys, J.-C. Bacri, C. Flament, S. Neveu and R. Perzynski, *Eur. Phys. J. B*, 1999, **9**, 335–341.

59 R. E. Zelazo and J. R. Melcher, *J. Fluid Mech.*, 1969, **39**, 1.

60 R. D. Deegan, O. Bakajin, T. F. Dupont, G. Huber, S. R. Nagel and T. A. Witten, *Nature*, 1997, **389**, 827–829.

61 Y. Yoneda, *Phys. Rev.*, 1963, **131**, 2010–2013.

62 Y. I. Dikansky, A. R. Zakinyan and L. S. Mkrtchyan, *Tech. Phys.*, 2010, **55**, 1270–1274.

63 J. Legrand, A. T. Ngo, C. Petit and M.-P. Pileni, *Adv. Mater.*, 2001, **13**, 58–62.

64 V. Germain and M.-P. Pileni, *Adv. Mater.*, 2005, **17**, 1424–1429.